

Role of intrinsic disorder in the structural phase transition of magnetoelectric EuTiO_3

Mattia Allietta,¹ Marco Scavini,^{1,*} Leszek J. Spalek,^{2,3} Valerio Scagnoli,^{4,5} Helen C. Walker,⁵ Christos Panagopoulos,^{2,3,6} Siddharth S. Saxena,² Takuro Katsufuji,⁷ and Claudio Mazzoli^{8,5}

¹*Dipartimento di Chimica Fisica ed Elettrochimica, Università degli Studi di Milano, Via Golgi 19, 20133 Milano, Italy*

²*Cavendish Laboratory, Madingley Road, Cambridge CB3 0HE, United Kingdom*

³*Department of Physics, University of Crete and FORTH, GR-71003 Heraklion, Greece*

⁴*Swiss Light Source, Paul Scherrer Institut, CH-5232 Villigen PSI, Switzerland*

⁵*European Synchrotron Radiation Facility, 6 rue Jules Horowitz, Boîte Postale 220, 38043 Grenoble Cedex 9, France*

⁶*Division of Physics and Applied Physics, Nanyang Technological University, Singapore*

⁷*Department of Physics, Waseda University, Tokyo 169-8555, Japan*

⁸*Politecnico di Milano, p.zza L. Da Vinci 32, I-20133 Milano, Italy*

(Received 2 November 2011; revised manuscript received 19 December 2011; published 18 May 2012)

Up to now, the crystallographic structure of the magnetoelectric perovskite EuTiO_3 has been considered to remain cubic down to low temperature. Here we present high-resolution synchrotron x-ray powder-diffraction data showing the existence of a structural phase transition, from cubic $Pm\bar{3}m$ to tetragonal $I4/mcm$, involving TiO_6 octahedra tilting, in analogy to the case of SrTiO_3 . The temperature evolution of the tilting angle and of the full width at half maximum of the (200) cubic reflection family indicate a critical temperature $T_c = 235$ K. This critical temperature is well below the recent anomaly reported by specific-heat measurement at $T_A \sim 282$ K. By performing atomic pair distribution function analysis on diffraction data, we provide evidence of a mismatch between the local (short-range) and the average crystallographic structures in this material. Below the estimated T_c , the average model symmetry is fully compatible with the local environment distortion, but the former is characterized by a reduced value of the tilting angle compared to the latter. At $T = 240$ K, data show the presence of local octahedra tilting identical to the low-temperature one, while the average crystallographic structure remains cubic. On this basis, we propose that intrinsic lattice disorder is of fundamental importance in the understanding of EuTiO_3 properties.

DOI: [10.1103/PhysRevB.85.184107](https://doi.org/10.1103/PhysRevB.85.184107)

PACS number(s): 64.70.K-, 75.80.+q, 61.05.cp, 77.80.-e

I. INTRODUCTION

Multiferroic materials attract a great deal of interest due to the complex phenomena arising from multiple coupled order parameters existing in a single system.¹ In the case of simultaneous ordering interplay, as in the subset of materials called magnetoelectrics, the control of ferroelectric polarization via a magnetic field² and of magnetic phases by an electric field³ has been proven to be possible.

The interplay of spin and other electronic or lattice degrees of freedom can induce giant magnetoelectric effects,^{4,5} dynamic behavior,⁶ as well as novel types of excitations,⁷ paving the way for future applications in sensors, data storage, and spintronics.^{8,9} In this paper, we present the case of magnetoelectric EuTiO_3 showing an unusual interplay between dielectric, magnetic, and structural degrees of freedom. At room temperature, its crystal structure has been reported to be $Pm\bar{3}m$ and no phase changes have been observed to occur down to 108 K,¹⁰ as deduced from lab source powder x-ray diffraction. From the dielectric point of view, EuTiO_3 is described as a quantum paraelectric, as its low-temperature dielectric constant increases on cooling and saturates below approximately 30 K.¹¹ No long-range polarization is known to set in, despite high values of susceptibility, typical of a paraelectric state stabilized by quantum fluctuations.¹² The localized $4f$ moments on the Eu^{2+} sites order at $T_N = 5.3$ K in an antiferromagnetic arrangement.¹³ Concomitant with the onset of antiferromagnetism, the dielectric constant decreases abruptly (by $\epsilon'_{5.5\text{K}}/\epsilon'_{2\text{K}} \sim 3.5\%$) and shows a strong enhancement as a function of the applied magnetic field ($\sim 7\%$

at $B \sim 1.5$ T), providing evidence for the magnetoelectric coupling.¹¹ In bulk magnetoelectrics, the coupling between various degrees of freedom is realized at a microscopic level,³ hence the crystallographic structure of EuTiO_3 as a function of temperature is vital to any further investigation and modeling. In this paper, we report on the structure of EuTiO_3 at low temperature, as given by high-resolution synchrotron x-ray powder-diffraction analysis. Since the diffraction experiments were performed, the authors have been made aware of a recent publication reporting on a specific-heat anomaly detected in EuTiO_3 powders at high temperature,¹⁴ and in our discussion we address the differences arising from different experimental probes.

II. EXPERIMENTS

High-quality EuTiO_3 samples have been grown by using the floating-zone method as outlined in Ref. 15. The growth procedure involves melting a pressed rod of mixed starting materials (Eu_2O_3 , Ti, and TiO_2) under an Ar atmosphere inside a floating-zone furnace. Polycrystalline samples coming from the same batches as the one used for x-ray measurements were checked by specific heat first, showing an anomaly identical to the one recently reported in the literature.¹⁴ EuTiO_3 crystals extracted from the inner part of the grown crystalline rod were powdered, loaded in a 0.70-mm-diam capillary, and spun during measurements to improve powder randomization. High-resolution powder-diffraction experiments were performed at the ID31 beamline of the European Synchrotron Radiation Facility (ESRF) by selecting a wavelength of $\lambda = 0.34986(1)$ Å.

Several samples were checked and a few selected on the basis of room-temperature x-ray powder-diffraction (XPD) measurements. The diffracted rays' full width at half maximum (FWHM) and symmetry criteria were applied to select a couple of the best samples: in the following, we report on measurements performed on those specimens. Different data collection strategies were employed: (i) in the $0 \leq 2\theta \leq 60^\circ$ range, data were collected for a total counting time of 2 h at room temperature, 240, 230, 215, 200, 175, 160, 140, 120, 100, and 80 K; (ii) in the $3 \leq 2\theta \leq 15^\circ$ range, 30 XPD patterns were collected while sweeping the temperature from 300 to 200 K; (iii) at 100 and 240 K, data were collected by summing several scans for a total counting time of 7 h ($Q_{\max} \sim 27 \text{ \AA}^{-1}$) to achieve the necessary quality for pair distribution function analysis.

The temperature on the sample was varied using a N_2 gas blower (Oxford Cryosystems) mounted coaxially to the sample capillary, being orthogonal to the scattering plane. Diffractograms were indexed by using the DICVOL91 software.¹⁶ Le Bail-type and Rietveld refinements were performed using the GSAS program.¹⁷ In particular, in the Rietveld refinement the background was fitted by Chebyshev polynomials. The absorption correction was performed through the Lobanov empirical formula¹⁸ implemented for the Debye-Scherrer geometry. In the last refinement cycles, scale factor, cell parameters, positional coordinates, and isotropic thermal parameters were allowed to vary as well as background and line profile parameters.

III. RIETVELD ANALYSIS

At room temperature, EuTiO_3 is isostructural to SrTiO_3 [space group $Pm-3m$, $a = 3.905 \text{ \AA}$ (Ref. 20)], and the Rietveld refinement of XPD patterns by the same cubic structural model^{10,19} leads to a satisfactory description of our data. Our lattice parameters agree well with the literature (this work: $a = 3.904782(5) \text{ \AA}$; Ref. 19: $a = 3.904 \text{ \AA}$). In Fig. 1(a), selected portions of the XPD patterns collected at various temperatures are shown. The contrast between the unperturbed

(111) reflection family and the (200) split one is evident. In particular, for this last reflection family, the intensity ratio of the two split peaks is $\sim 1/2$, suggesting a cubic to tetragonal structural phase transition.

To solve the low-temperature structure, we have concentrated on XPD data collected at 100 K. First of all, 20 strong independent peaks were indexed, resulting in a tetragonal unit cell of lattice parameters $a, b = 3.896 \text{ \AA}$, $c = 3.903 \text{ \AA}$. Then, by using a Le Bail-type profile matching without structural model, based on the holohedral space group $P4/mmm$, we detected the presence of a few nonindexed weak reflections, as shown in Fig. 1(b). A search for possible supercells gave a unit cell with lattice parameters of $a, b = 5.509 \text{ \AA}$, $c = 7.808 \text{ \AA}$, and the analysis of systematic extinctions for this cell was compatible with a body-centered lattice. The two previous tetragonal cells are related according to the transformation matrix $(1,1,0)$, $(-1,1,0)$, $(0,0,2)$, or, alternatively, the low-temperature tetragonal supercell can be classified as a pseudocubic cell with unit-cell metric $\sqrt{2}a \times \sqrt{2}a \times 2a$, where a is the primitive cubic perovskite lattice parameter. By using the Le Bail-type refinement procedure, we fitted the diffractograms acquired below room temperature with the new cell metric. In Fig. 2, we present the refined lattice parameters as a function of temperature for EuTiO_3 together with x-ray diffraction data obtained for SrTiO_3 ,²¹ where a reduced tetragonal cell metric was used for comparison purposes between the cubic and tetragonal phases in the two systems. Figure 2 clearly shows similarities between EuTiO_3 and SrTiO_3 . The latter was shown to exhibit a second-order displacive phase transition below $T_c = 106 \text{ K}$,²² so quite naturally we started from this hypothesis in the analysis of EuTiO_3 structural phase transition. The possible mechanisms accounting for such a modulation of the aristotype perovskite structure ($Pm-3m$) can be generated by a Jahn-Teller distortion,²³ a tilting of corner-linked BO_6 octahedral units,^{24,25} polar distortions,²⁵ or higher-order mechanisms coupling several of these.²⁶ Given the electronic state of Ti in EuTiO_3 ($3d^0$),²⁷ we concentrated on octahedral tilting, and group-theoretical methods have been applied in order

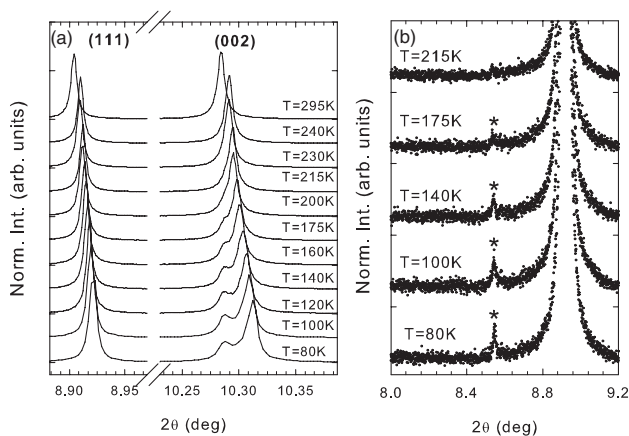


FIG. 1. Selected 2θ regions of EuTiO_3 x-ray diffraction patterns are shown as a function of temperature. (a) The temperature evolution of the Miller index (111) and (002) peaks related to the room-temperature cubic phase. (b) The appearance of a weak superlattice reflection as a function of temperature.

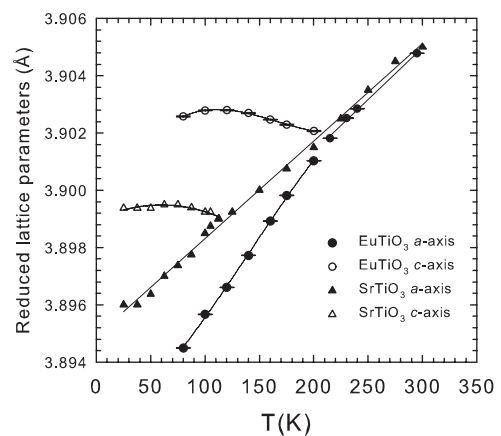


FIG. 2. Reduced lattice parameters of EuTiO_3 and SrTiO_3 as a function of temperature. The full and opened circles are the a and c axes of EuTiO_3 . Full and opened triangles indicate the a - and c -axis values of SrTiO_3 derived from Ref. 21. The continuous lines are guides to the eye.

to classify compatible structures assuming a second-order phase transition. The analysis yielded a list of 15 possible space groups,²⁵ subgroups of the high-temperature cubic one. Restraining the analysis to tetragonal space groups,²⁵ the possible choices are as follows (between parentheses is the related cell):²⁸ $I4/mmm$ ($2a \times 2a \times 2a$), $P4/mbm$ ($\sqrt{2}a \times \sqrt{2}a \times 2a$), $I4/mcm$ ($\sqrt{2}a \times \sqrt{2}a \times 2a$), and $P4_2/nmc$ ($2a \times a \times 2a$). Space groups related to a $2a \times 2a \times 2a$ cell, i.e., $I4/mmm$ and $P4_2/nmc$, are incompatible with the data on the basis of the metrics (i.e., indexation of the peaks due to the supercell structure). Moreover, $P4_2/nmc$ has special extinction conditions, not fulfilled by the experimental pattern. The $P4/mbm$ space group is completely ruled out by both the metrics and the lattice type. These arguments leave $I4/mcm$ as the only possibility. The tetragonal structure in the $I4/mcm$ space group is consistent with an out-of-phase tilting of octahedra around the tetragonal axis. The associated irreducible representation (irrep) is R_4^+ .²⁵ The direction of the distortion in the irrep space is indicated by the vector $(a,0,0)$. To obtain the starting atomic positions in $I4/mcm$, the ISOTROPY²⁹ package was used on the basis of the Wyckoff sites occupied in the undistorted cubic structure: Ti on $1a$ $(0, 0, 0)$, Eu on $1b$ $(\frac{1}{2}, \frac{1}{2}, \frac{1}{2})$, and O on $3d$ $(\frac{1}{2}, 0, 0)$. The asymmetric unit of the $I4/mcm$ subgroup consists then of Ti at $4c$ $(0, 0, 0)$, Eu at $4b$ $(0, \frac{1}{2}, \frac{1}{4})$, O1 at $4a$ $(0, 0, \frac{1}{4})$, and O2 at $8h$ $(x, x + \frac{1}{2}, 0)$ with $x \sim \frac{1}{4}$. Figure 3 shows the Rietveld refinement of data collected at 100 K, as obtained by using the above structural model in the $I4/mcm$ space group. In Table I, structural data and agreement factors obtained for patterns collected at different temperatures are listed. In the tetragonal phase, we constrained both isotropic thermal parameters related to oxygen positions O1 and O2 to be the same. The thermal variation of the Ti-O and Eu-O bond lengths is given in Figs. 4(a) and 4(b). In the cubic phase, the Ti-O1 distance decreases

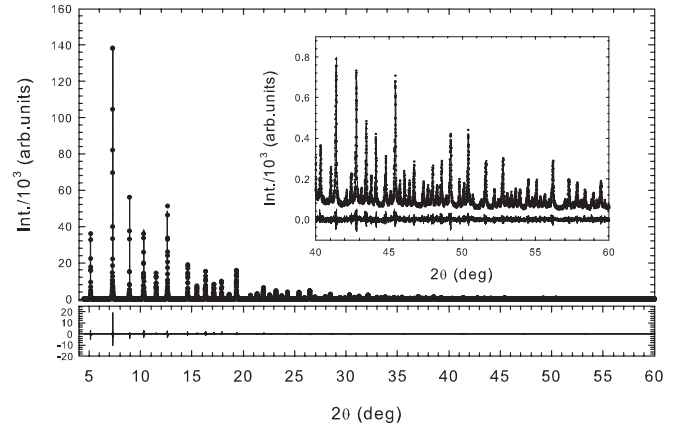


FIG. 3. Measured (dots) and calculated (lines) powder-diffraction patterns for EuTiO_3 at 100 K. The inset shows a magnified view of the high-angle diffraction peaks. The difference between the observed and fitted patterns is displayed at the bottom of each figure.

with decreasing temperature. Below 215 K, according to the tilting of TiO_6 octahedra, Ti-O distances visibly split as a result of oxygen basal plane O2 displacement. Moreover, it should be noted that since in the tetragonal phase the Ti-O1 indicates the distance between Ti and the apical O1 position of octahedron, its thermal variation follows the c -axis length evolution on cooling (see Fig. 2). The Eu-O1 distance remains approximately constant within the temperature range studied. In the tetragonal phase, short (Eu-O2) and long (Eu-O2') distances are generated by the displacement of the O2 position. In perovskites, the out-of-phase tilting angle of TiO_6 octahedra (ϕ_-), as calculated from the refined values of the $x[\text{O}(2)]$ position, according to $\tan \phi_- = 1 - 4x[\text{O}(2)]$,³⁰ has been proposed as the primary order parameter of the $Pm-3m$ to

TABLE I. Refined structural data of EuTiO_3 obtained from synchrotron x-ray powder diffraction.

T (K)	293	240	230	215	200	175
a (Å)	3.904782(5)	3.902847(3)	3.902521(2)	3.901813(3)	5.516890(7)	5.515173(8)
c (Å)					7.804140(3)	7.804589(3)
$U(\text{Eu})$ (Å ²)	0.00748(3)	0.00655(2)	0.00623(2)	0.00593(2)	0.00507(2)	0.00471(2)
$U(\text{Ti})$ (Å ²)	0.00454(6)	0.00400(6)	0.00389(6)	0.00373(6)	0.00335(5)	0.00315(5)
$U(\text{O})$ (Å ²)	0.0106(2)	0.0105(2)	0.0101(2)	0.0107(2)	0.0092(2)	0.0090(2)
$x[\text{O}(2)]$					0.2439(7)	0.2410(6)
ϕ (°)					1.41(17)	2.06(14)
R_{wp}	0.1023	0.1073	0.1069	0.1100	0.0864	0.0945
$R(F^2)$	0.0452	0.0422	0.0400	0.0427	0.0251	0.0268
χ^2	4.494	5.886	5.722	5.117	4.011	3.622
T (K)	160 K	140 K	120 K	100 K	80 K	
a (Å)	5.513909(8)	5.512217(6)	5.510639(6)	5.509309(6)	5.507642(9)	
c (Å)	7.804941(28)	7.805394(21)	7.805601(6)	7.805572(20)	7.805161(25)	
$U(\text{Eu})$ (Å ²)	0.00445(2)	0.00407(2)	0.00366(2)	0.00325(1)	0.00252(2)	
$U(\text{Ti})$ (Å ²)	0.00302(5)	0.00284(5)	0.00270(4)	0.00251(4)	0.00220(4)	
$U(\text{O})$ (Å ²)	0.0086(2)	0.0084(2)	0.0079(2)	0.0074(2)	0.0073(2)	
$x[\text{O}(2)]$	0.2399(5)	0.2384(4)	0.2373(4)	0.2363(4)	0.2353(4)	
ϕ (°)	2.30(12)	2.66(10)	2.92(9)	3.14(8)	3.35(9)	
R_{wp}	0.0944	0.0942	0.0934	0.0945	0.0941	
$R(F^2)$	0.0273	0.0271	0.0274	0.0268	0.0258	
χ^2	3.809	4.010	4.208	4.578	4.847	

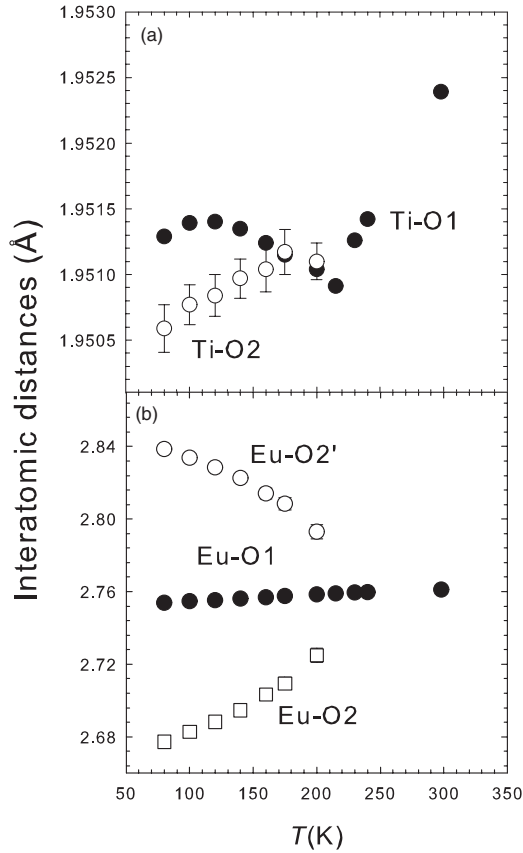


FIG. 4. (a), (b) The refined Ti-O and Eu-O interatomic distances as a function of temperature.

$I4/mcm$ displacive transition of the average structural model. Figure 5 shows the values obtained from our refinements as a function of temperature, as listed in Table I. We fitted the temperature dependence of ϕ_- by using the equation $\phi_-(T) = \phi_-(0)(1 - T/T_c)^\beta$. By setting $T_c = 215$ K, we obtained the parameters $\phi_-(0) = 4.03(2)^\circ$ and $\beta = 0.40(1)$. As shown in Fig. 5 by the solid line, the fit is reasonably good, providing

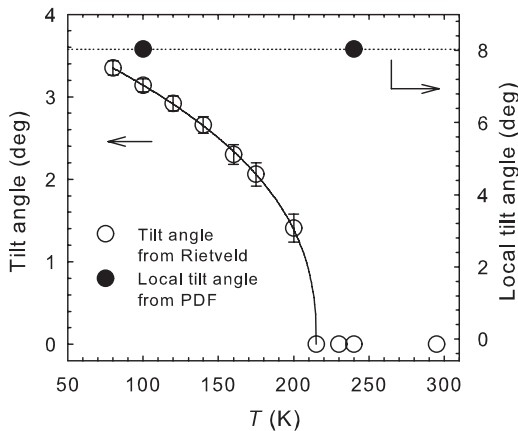


FIG. 5. EuTiO_3 octahedral tilting angle values (empty circles) as a function of temperature obtained from the Rietveld refinement (Table I). The continuous line is the best fit for the critical equation $\phi_-(T) = \phi_-(0)(1 - T/T_c)^\beta$, by setting $T_c = 215$ K. The full circles are the tilting angle values obtained from PDF refinements (Table II).

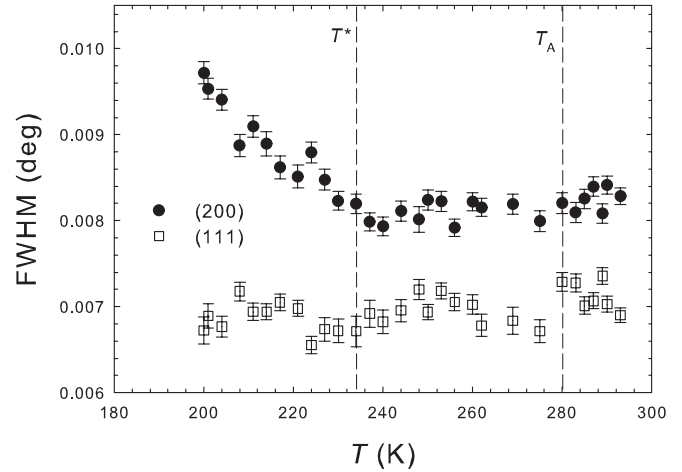


FIG. 6. Temperature evolution of the (200) and (111) Bragg families FWHM for the cubic phase of EuTiO_3 .

evidence of the continuous nature of the temperature evolution of ϕ_- .

Recently, an anomaly in the temperature dependence of specific heat measured on a powdered EuTiO_3 sample has been reported, suggesting a structural instability at $T_A = 282(1)$ K.¹⁴ Moreover, theoretical calculation performed by the same authors predicts a second-order antiferrodistortive phase transition which agrees perfectly with the $Pm-3m$ to $I4/mcm$ transition reported here. Despite this agreement, the discrepancy between the T_c estimated from data in Fig. 5(a) and the reported $T_A = 282(1)$ K (Ref. 14) requires further investigation. For this reason, we performed an accurate profile analysis of the (200) reflection indexed within a cubic unit cell [Fig. 1(a)] on the 30 XPD patterns collected between 200 and 300 K. In Fig. 6, we report the FWHM of the (200) cubic reflection family as a function of temperature. In each pattern, a single profile function was used because any attempt to describe the (200) peak by using multiple peaks resulted in unphysical fluctuations of the fitting parameters. For the sake of comparison, the temperature dependence of the FWHM related to the (111) cubic reflection family is also shown. The FWHM of (200) smoothly increases on cooling below $T^* \sim 235$ K (Fig. 6). This suggests that the structural distortion inducing the FWHM variation occurs at higher temperature than the temperature estimated by the previous method. However, we point out that from the point of view of XPD at 235 K, the structural phase transition is just *incipient* without causing a detectable symmetry breaking until ~ 200 K is reached. Indeed, the splitting of the cubic (200) peak is not visible in the $200 \leq T \leq 235$ K range, the difference in the average (see below) d space induced by the tetragonal distortion falling below the instrument resolution. It should be noted that a similar behavior was already reported by some of the present authors concerning the tetragonal-to-orthorhombic transition of rare-earth cobaltite perovskite.³¹

However, $T^* \sim 235$ K is still too low to be consistent with the reported T_A from specific-heat measurements.¹⁴ Such a discrepancy can arise from an incomplete description of the structural phase-transition mechanism or because of intrinsic limits characteristic of the investigation technique. Among

functional materials, like EuTiO_3 ,³² a general consensus is growing on the relation between physical properties of interest and disorder occurring at the local scale.³³ In the case of phase inhomogeneity, for example, the local and the average crystallographic structures are expected to differ, the correlation length of the structural distortion being spatially limited. If so, conventional analysis of XPD data, such as the Rietveld method, can be inadequate,³⁴ being able to detect only sufficiently long structural correlations (average structure). On the contrary, total scattering methods, such as the pair distribution function (PDF), have been successfully applied to similar problems in Ti-based perovskites.^{35,36}

IV. PDF ANALYSIS

We carried out a PDF analysis of the XPD data collected at $T = 100$ and 240 K. The PDF function $G(r)$ is obtained through the total structure factor $S(Q)$ via the sine Fourier transform (FT):

$$\begin{aligned} G(r) &= 4\pi r[\rho(r) - \rho_0] \\ &= \frac{2}{\pi} \int_{Q=0}^{Q_{\max}} Q[S(Q) - 1] \sin(Qr) dQ, \end{aligned} \quad (1)$$

where $Q_{\max} = 4\pi \sin\theta/\lambda$, $\rho(r)$ and ρ_0 are the local and average atomic number densities, r is the interatomic distance, and the total structure factor $S(Q)$ is obtained from the experimental coherent x-ray scattering intensity $I^{\text{coh}}(Q)$ according to

$$S(Q) - 1 = \frac{I^{\text{coh}}(Q) - \langle f^2(Q) \rangle}{\langle f(Q) \rangle^2}. \quad (2)$$

Here $f(Q)$ is the atomic scattering factor and the angular brackets denote the average over the compound unit. To evaluate $I^{\text{coh}}(Q)$ consistently, the raw diffracted intensity $I(Q)$ collected at each temperature was corrected for background scattering, attenuation in the sample, and multiple and Compton scattering. In particular, at high Q the Compton scattering was removed by calculating the Compton profile with an analytical formula. In the middle-low Q region, the Compton scattering correction was applied by multiplying the calculated Compton profile with a monochromator cutoff function.³⁴ The corrected $I(Q)$ were then properly normalized, converted to get $S(Q)$, and Fourier-transformed according to Eq. (1) to obtain the PDF data. The reduction operations have been done using the PDFGETX2 software.³⁷ Full structure profile refinements were carried out on the PDF data using the PDFGUI program.³⁸ The program assesses the degree of accuracy of the refinement by the following agreement factor:

$$R_W = \left[\frac{\sum w_i (G_i^{\text{exp}} - G_i^{\text{calc}})^2}{\sum w_i (G_i^{\text{exp}})^2} \right]^{1/2}. \quad (3)$$

Data collected were analyzed starting from $r = 2.3$ Å, i.e., excluding the shortest Ti-O distances. Indeed, the total $G(r)$ can be expressed as the sum of the partial $g_{i-j}(r)$ weighted for the atomic fractions and $f(Q)$ of the i and j components. Given the contrast between the x-ray scattering factors of the element pairs involved, i.e., Eu-Eu, Eu-Ti, Eu-O, Ti-Ti, and Ti-O, the partial $g_{\text{Ti-O}}(r)$ has the lowest weighting. Then, at very low r , the $G(r)$ peak related to the Ti-O pair corresponds

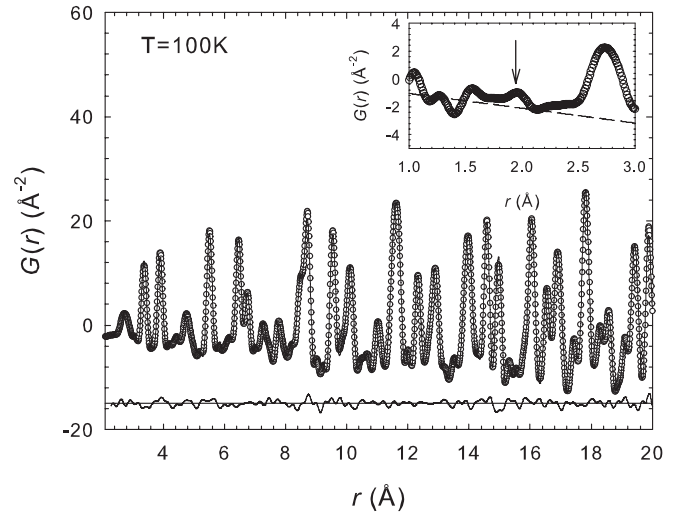


FIG. 7. Observed (dots) and calculated (continuous line) PDF obtained for EuTiO_3 at 100 K. The residual plot is shown at the bottom of the figure. In the inset, a region of short interatomic distances is displayed. The dashed line is the baseline and corresponds to $-4\pi r\rho_0$ [see Eq. (1)]. The arrow indicates approximately the r position of Ti-O interatomic distances.

to a very weak feature with respect to the baseline ($-4\pi r\rho_0$), as shown by the arrow in the inset of Fig. 7. PDF analysis is sensitive to different crystallographic correlation lengths via the refined range of the interatomic distance r . Figure 7 shows the full PDF profile structural refinement obtained at 100 K by using the average $I4/mcm$ model in the $2.3 \leq r \leq 20$ Å range. The agreement factor obtained ($R_W = 0.073$) confirms the good quality of the fit at low enough temperatures when describing local distortions by the average model. Table II lists the structural parameter resulting from the PDF refinement at 100 K. By considering U(O1) and U(O2) unrelated, we obtain a marked improvement of the fit quality, so that all the reported PDF refinements were performed without oxygen thermal motion constraints. In the following, the proposed structural order parameter ϕ_- , as obtained by both Rietveld and PDF refinement, is compared as a function of r . As reported in Table II, for $2.3 \leq r \leq 20$ Å (short-range) PDF analysis gives a structural order parameter of $\phi_- = 8.05(4)^\circ$, while for $20 \leq r \leq 50$ Å (long-range) a value of $\phi_- = 3.3(1)^\circ$ is obtained, showing a strong dependence of the tilting angle as a function of the interatomic distance. In addition, the ϕ_- value found above 20 Å is in close agreement with the value obtained from Rietveld analysis of the XPD data [$\phi_- = 3.14(8)^\circ$]. Figure 8 shows the short-range portion of the PDF refinement at 240 K. In panel (a), the average $Pm-3m$ cubic model is shown. The calculated PDF systematically underestimates the intensity of most of the experimental peaks, proving the undistorted model to be inadequate. In panel (b), the fit performed by using the $I4/mcm$ model in the same r range is shown. $I4/mcm$ has a better agreement with the data and the marked features in panel (a) are now well described. Conversely, as shown in Fig. 9, by comparing the fittings performed in the high r region ($r > 20$ Å) using both the cubic and tetragonal, we found that the $Pm-3m$ structural model gives a reasonable fit over the long-range part. Moreover, it should be noted that by using

TABLE II. Refined structural parameters of EuTiO_3 obtained from PDF refinements at 100 and 240 K.

T (K)	100 K		240 K			
	$I4/mcm$		$Pm-3m$		$I4/mcm$	
S. G.	$I4/mcm$		$Pm-3m$		$I4/mcm$	
Range	$2.3 \leq r \leq 20 \text{ \AA}$	$20 \leq r \leq 50 \text{ \AA}$	$2.3 \leq r \leq 20 \text{ \AA}$	$20 \leq r \leq 50 \text{ \AA}$	$2.3 \leq r \leq 20 \text{ \AA}$	$20 \leq r \leq 50 \text{ \AA}$
$a/\text{\AA}$	5.5124(1)	5.5088(2)	3.9019(5)	3.9022(1)	5.5197(8)	5.5180(2)
$c/\text{\AA}$	7.7931(8)	7.8030(5)			7.8002(2)	7.8060(7)
$U(\text{Eu})/\text{\AA}^2$	0.003225(6)	0.003905(2)	0.005463(2)	0.006785(2)	0.005794(2)	0.006648(2)
$U(\text{Ti})/\text{\AA}^2$	0.004317(6)	0.005831(4)	0.006056(5)	0.007231(3)	0.006228(5)	0.007166(3)
$U(\text{O1})/\text{\AA}^2$	0.00341(2)	0.006988(3)	0.02470(5)	0.02594(2)	0.00366(1)	0.00562(2)
$U(\text{O2})/\text{\AA}^2$	0.0429(4)	0.0514(4)			0.0449(2)	0.0570(2)
$x[\text{O}(2)]$	0.2147(2)	0.2356(6)			0.2147(1)	0.2432(7)
ϕ ($^\circ$)	8.05(4)	3.3(1)			8.04(2)	1.6(2)
R_W	0.073	0.074	0.107	0.079	0.074	0.070

the tetragonal model at high r , we found a strong correlation among the model parameters (in particular between a and c lattice parameters and $x[\text{O}(2)]$ and $U(\text{O}2)$) and an agreement factor R_W very similar to that of cubic fit (Table II), despite

the increased number of variable parameters.. This indicates that EuTiO_3 completely recovers its average structure already at interatomic distances of $\sim 20 \text{ \AA}$ and provides clear evidence of a mismatch between the short- and the long-range structure at a temperature as high as $T = 240 \text{ K}$.

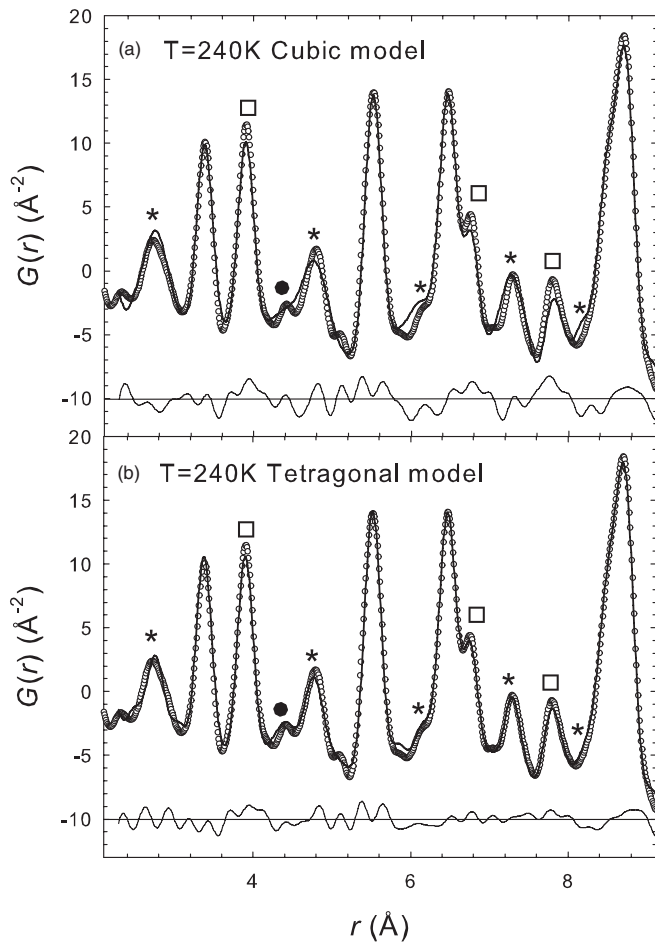


FIG. 8. Short-range observed (dots) and calculated (continuous lines) PDF for EuTiO_3 at 240 K. (a) and (b) are the fits obtained using the cubic *average* model and the low-temperature tetragonal model, respectively. The symbols in the panel label the PDF peaks belonging to Eu-O (stars), Eu-Eu (empty squares), and Ti-O (full circles) interatomic distances.

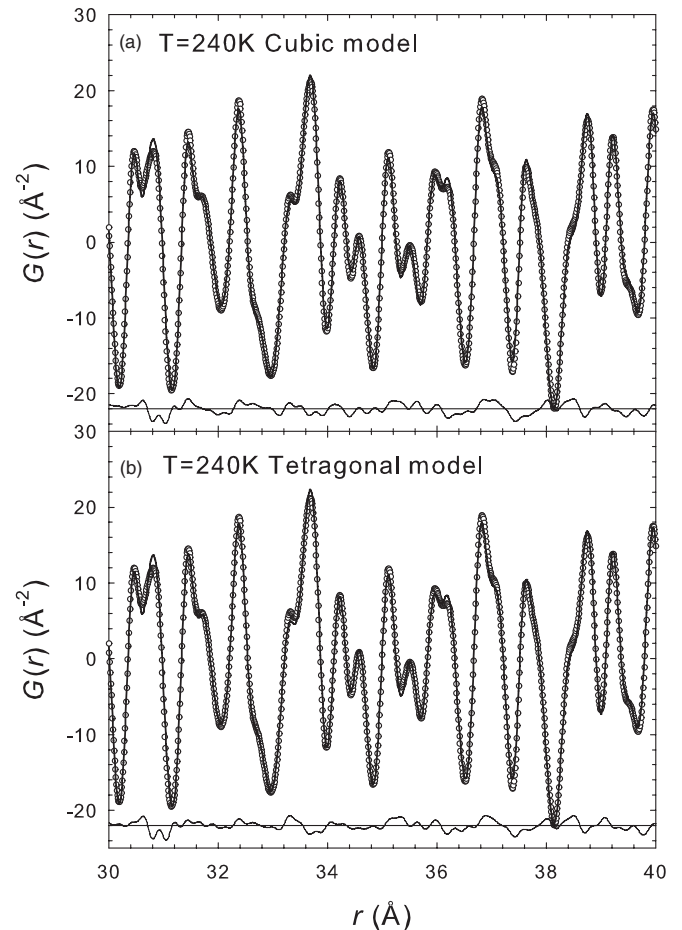


FIG. 9. Observed (dots) and calculated (continuous lines) high- r PDF for EuTiO_3 at 240 K. (a) and (b) are the fits obtained using the cubic *average* model and low-temperature tetragonal model, respectively.

V. DISCUSSION

PDF analysis of powder-diffraction patterns suggests EuTiO_3 to be an intrinsically disordered system, as a clear mismatch between the short- and long-range crystallographic structures is evident at 240 K. At 100 K, the long-range tetragonal model describes the short-range PDF well qualitatively, but an increased value of the tilting angle is necessary to properly fit the data. In order to reconcile the discrepancy in the T^* and T_A scales of the temperature anomalies, we propose the following picture involving the structural findings of EuTiO_3 . According to specific-heat measurement interpretation,¹⁴ a second-order phase transition occurs in EuTiO_3 at $T_A \sim 282$ K. On the basis of the low-temperature structural refinement shown above, we tentatively attribute this anomaly to a $Pm-3m$ to $I4/mcm$ displacive structural transition. The outcome of our PDF analysis at 240 K shows how the correlation length of the tetragonal $I4/mcm$ phase remains confined at the nanoscopic scale (~ 20 Å) and we suppose this structure to be stable in the range $\sim 235 \leq T \leq 282$ K. Conversely, in the same T range, the XPD data imply that the structure is cubic. A possible explanation to account for such a mismatch implies that the tilting changes randomly from one nanoregion to the adjacent one. This quickly averages out the metric variation on a longer scale, i.e., the crystallite size, and reduces the average structure to a cubic space group. By decreasing T , we suppose that a divergence of the correlation length of the tetragonal distortion takes place. This results in a disorder-order transition at $T^* \sim 235$ K. Our observations (see Fig. 6) suggest that close to T^* , the magnitude of the tetragonal distortion corresponding to the long-range ordered phase is still small, so that the transition shows up just as a weak feature in the temperature dependence of the cubic (200) FWHM. Upon further cooling, the tetragonal deviation from the cubic metric increases until the experimental resolution is finally sufficient to resolve it below 215 K. There, splitting of the Bragg peaks as well as the appearance of superlattice reflections are clearly observed in Rietveld refinements. It is worth noticing that even at $T = 100$ K, i.e., well below T^* , the local tilting angle is greater than the one obtained from the long-range PDF refinement. At $T = 100$ and 240 K, the local tilting angles (short-range refinement) are the same ($\sim 8^\circ$), see Fig. 5 and Table II, whereas the tilting angle obtained at $T = 100$ K from the long-range PDF refinement agrees well with the result of the Rietveld refinement for the average structure ($\sim 3^\circ$). On the other hand, C_p measurements do not show a sharp feature but a quite broad one over the temperature range shown in Ref. 14, leaving the possibility of a further evolution of the structural distortion correlation length possible. In principle, the space group $I4cm$ obtained from the coupling of R_4^+ and the Γ_4^+ polar irreducible representation²⁵ could be compatible with our experimental results on the basis of metrics and extinction conditions.³⁹ In this case, a strong dynamical behavior of the dielectric constant would be expected, and given the mismatch between the local and the long-range orders found in EuTiO_3 , the system could act as a relaxor ferroelectric.⁴⁰ In these systems, the disorder is typically introduced extrinsically through chemical doping, while in EuTiO_3 the structure itself seems to be willing to organize at a nanoscopic scale (forming domains of the order of ~ 20 Å).

To validate the suggested mechanism, a detailed study of the temperature evolution of the local structure of EuTiO_3 around the critical temperatures must be performed. Complementary temperature-dependent neutron PDF experiments would be more informative to clarify how the correlation length of the tetragonal distortion affects the physics of EuTiO_3 , but they are hindered by the large Eu neutron absorption cross section.

VI. CONCLUSIONS

In conclusion, in this paper we show, on the basis of XPD data analysis, that EuTiO_3 undergoes a cubic to tetragonal structural phase transition below room temperature. The $I4/mcm$ space group, generated by an out-of-phase tilting of TiO_6 octahedra, gives the best description of our powder-diffraction data at low temperatures. Specific-heat measurements in the literature show an anomaly at $T_A = 282(1)$ K. Our PDF analysis of XPD data shows that at $T = 240$ K, the structure of EuTiO_3 is already distorted and consistent with the presence of local tilting regions embedded in a long-range cubic phase. From Rietveld analysis of XPD data, the temperature dependence of the average tilting angle and of the (200) cubic peak FWHM suggests a continuous transition taking place at $T^* \sim 235$ K. From the comparison between the Rietveld and the PDF analysis of XPD data, we propose that the difference between T^* and T_A is due to the correlation length scale evolution of the structural phase transition. Moreover, at $T = 100$ K the average model is consistent with the outcome of the long-range PDF refinement, while the short-range one suggests that a bigger value of the tilting angle is locally realized. This provides evidence of disorder at the nanometric scale even below T^* , suggesting EuTiO_3 to be an intrinsically disordered system in which the structural phase correlation length changes dramatically over a wide range of temperatures. In the case of a further symmetry breaking of the $I4/mcm$ space group by inversion symmetry loss, a possibility that cannot be excluded by the present investigation, this material would represent evidence of an intrinsic relaxor magnetoelectric: disorder-modulated interactions are expected to deeply influence the low-temperature electric properties. For the above reason, we believe that this fact has to be taken into suitable consideration when describing the peculiar properties of ETO as a quantum paraelectric material.

ACKNOWLEDGMENTS

The authors gratefully acknowledge the European Synchrotron Radiation Facility for provision of beam time and Adrian Hill for assistance in using the ID31 beamline. Some of the authors would also like to thank O. Petrenko, J. Scott, and P. Nahai-Williamson for useful discussions. We acknowledge also the financial support by the European Union through MEXT-CT-2006-039047, EURYI research grants, by the EPSRC and Jesus College, FCO Global Opportunities Fund and by the Swiss National Science Foundation, NCCR MaNEP. The work in Singapore was supported by the National Research Foundation.

*marco.scavini@unimi.it

- ¹W. Eerenstein, N. D. Mathur, and J. F. Scott, *Nature (London)* **442**, 759 (2006).
- ²T. Kimura, T. Goto, H. Shintani, K. Ishizaka, T. Arima, and Y. Tokura, *Nature (London)* **426**, 55 (2005).
- ³T. Lottermoser, T. Lonkai, U. Amann, D. Hohlwein, J. Ihlinger, and M. Fiebig, *Nature (London)* **430**, 541 (2004).
- ⁴J. Wang, H. Zheng, V. Nagarajan *et al.*, *Science* **299**, 1719 (2003).
- ⁵A. Zvezdin and A. Pyatakov, *Usp. Fiz. Nauk* **174**, 465 (2004).
- ⁶J. Hemberger, P. Lunkenheimer, R. Fichtl, H.-A. K. von Nidda, V. Tsurkan, and A. Loidl, *Nature (London)* **434**, 364 (2005).
- ⁷A. Pimenov, A. A. Mukhin, V. Y. Ivanov, V. D. Travkin, A. M. Balbashov, and A. Loidl, *Nat. Phys.* **2**, 97 (2006).
- ⁸J. Scott, *Nat. Mater.* **6**, 256 (2007).
- ⁹A. Zvezdin, A. Logginov, G. Meshkov, and A. Pyatakov, *Bull. Rus. Acad. Sci.* **71**, 1561 (2007).
- ¹⁰J. Brous, I. Fankuchen, and E. Banks, *Acta Cryst.* **6**, 67 (1953).
- ¹¹T. Katsufuji and H. Takagi, *Phys. Rev. B* **64**, 054415 (2001).
- ¹²K. A. Muller and C. T. Burkard, *Phys. Rev. B* **19**, 3593 (1979).
- ¹³T. R. McGuire, M. W. Shafer, R. J. Joenk, H. A. Alperin, and S. J. Pickart, *J. Appl. Phys.* **37**, 981 (1966).
- ¹⁴A. Bussmann-Holder, J. Köhler, R. K. Kremer, and J. M. Law, *Phys. Rev. B* **83**, 212102 (2011).
- ¹⁵T. Katsufuji and Y. Tokura, *Phys. Rev. B* **60**, R15021 (1999).
- ¹⁶A. Boulouf and D. Louer, *J. Appl. Cryst.* **24**, 987 (1991).
- ¹⁷A. Larson and R. Von Dreele, Los Alamos National Laboratory Report LAUR (2004), pp. 86–748.
- ¹⁸N. N. Lobanov and L. Alte da Veiga, 6th European Powder Diffraction Conference, Abstract P12–16, Aug. 22–25, 1998.
- ¹⁹D. L. Janes, R. E. Bodnar, and A. L. Taylor, *J. Appl. Phys.* **49**, 1452 (1978).
- ²⁰F. W. Lytle, *J. Appl. Phys.* **35**, 2212 (1964).
- ²¹A. Okazaki and M. Kawaminami, *Mater. Res. Bull.* **8**, 545 (1973).
- ²²H. Unoki and T. Sakudo, *J. Phys. Soc. Jpn.* **23**, 546 (1967).
- ²³M. A. Carpenter and C. J. Howard, *Acta Crystallogr. Sect. B* **65**, 134 (2009).
- ²⁴C. J. Howard and H. T. Stokes, *Acta Crystallogr. Sect. B* **54**, 782 (1998).
- ²⁵C. J. Howard and H. T. Stokes, *Acta Crystallogr. Sect. A* **61**, 93 (2005).
- ²⁶H. T. Stokes, E. H. Kisi, D. M. Hatch, and C. J. Howard, *Acta Crystallogr. Sect. B* **58**, 934 (2002).
- ²⁷C.-L. Chien, S. De Benedetti, and F. De S. Barros, *Phys. Rev. B* **10**, 3913 (1974).
- ²⁸The unit cell metrics are expressed as multiplied periodicity of the $Pm-3m$ parent ($a \times a \times a$).
- ²⁹H. T. Stokes, D. M. Hatch, and B. J. Campbell, ISOTROPY (2007), <http://stokes.byu.edu/isotropy.html>.
- ³⁰K. Tsuda and M. Tanaka, *Acta Crystallogr. A* **51**, 7 (1995).
- ³¹L. LoPresti, M. Allieta, M. Scavini, P. Ghigna, L. Loconte, V. Scagnoli, and M. Brunelli, *Phys. Rev. B* **84**, 104107 (2011).
- ³²J. H. Lee *et al.*, *Nature (London)* **466**, 954 (2010).
- ³³E. Dagotto, *Science* **309**, 257 (2005).
- ³⁴T. Egami and S. J. L. Billinge, *Underneath the Bragg Peaks: Structural Analysis of Complex Materials*, Pergamon Materials Series, Vol. 7 (Pergamon, Oxford, 2003).
- ³⁵K. Page, T. Kolodiazny, T. Proffen, A. K. Cheetham, and R. Seshadri, *Phys. Rev. Lett.* **101**, 205502 (2008).
- ³⁶J.-C. Zheng, A. I. Frenkel, L. Wu, J. Hanson, W. Ku, E. S. Božin, S. J. L. Billinge, and Y. Zhu, *Phys. Rev. B* **81**, 144203 (2010).
- ³⁷X. Qiu, J. W. Thompson, and S. J. L. Billinge, *J. Appl. Crystallogr.* **37**, 678 (2004).
- ³⁸C. L. Farrow, P. Juhás, J. W. Liu, D. Bryndin, E. S. Božin, J. Bloch, Th. Proffen, and S. J. L. Billinge, *J. Phys.: Condens. Matter* **19**, 335219 (2007).
- ³⁹By considering [001] as the polar direction and the Eu position (i.e., the Γ_4^+ polar irreducible representation) as a reference, we refined the data using the $I4cm$ model. By comparing the results from $I4/mcm$ and $I4cm$ models, we found no improvement in the refinement statistics at any temperature. However, it is worth noting that the discrimination between the $4/mmm$ and $4mm$ point symmetries requires a careful examination of the intensity distribution statistics, a very difficult task to be performed on powder-diffraction data due to peak overlapping. Hence, the occurrence of inversion symmetry breaking cannot be unequivocally excluded by the current analysis of our high-resolution XPD data.
- ⁴⁰I.-K. Jeong, T. W. Darling, J. K. Lee, Th. Proffen, R. H. Heffner, J. S. Park, K. S. Hong, W. Dmowski, and T. Egami, *Phys. Rev. Lett.* **94**, 147602 (2005).